

# Probing Structural and Motional Features of the C-Terminal Part of the Human Centrin 2/P17-XPC Microcrystalline Complex by Solid-State NMR Spectroscopy

Jose-Enrique Herbert-Pucheta,<sup>†,‡,§</sup> Monique Chan-Huot,<sup>†,‡,§,||,⊥</sup> Luminita Duma,<sup>†,‡,§</sup> Daniel Abergel,<sup>†,‡,§</sup> Geoffrey Bodenhausen,<sup>†,‡,§</sup> Liliane Assairi,<sup>||,⊥</sup> Yves Blouquit,<sup>||,⊥</sup> Jean-Baptiste Charbonnier,<sup>#</sup> and Piotr Tekely<sup>\*,†,‡,§</sup>

<sup>†</sup>Ecole Normale Supérieure, Département de Chimie, 24 rue Lhomond, 75231 Paris, France

<sup>‡</sup>Université Pierre-et-Marie Curie, Paris, France

<sup>§</sup>UMR 7203, Laboratoire des Biomolécules, CNRS/UPMC/ENS, Paris, France

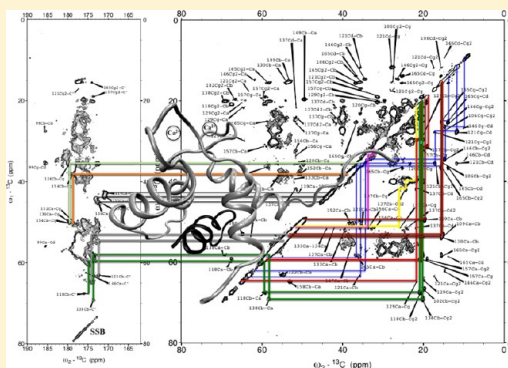
<sup>||</sup>Institut Curie - Centre de Recherche, 91405 Orsay, France

<sup>⊥</sup>INSERM U759, 91405 Orsay, France

<sup>#</sup>UMR 8221, Laboratoire de Biologie Structurale et Radiobiologie, iBiTec-S, CEA, 91191 Gif-sur-Yvette, France

## Supporting Information

**ABSTRACT:** Insight into structural and motional features of the C-terminal part of the Human Centrin 2 in complex with the peptide P17-XPC was obtained by using complementary solid-state NMR methods. We demonstrate that the experimental conditions and procedures of sample crystallization determine the quality of solid-state NMR spectra and the internal mobility of the protein. Two-dimensional (2D)  $^{13}\text{C}$ – $^{13}\text{C}$  and  $^{15}\text{N}$ – $^{15}\text{N}$  correlation spectra reveal *intra*- and *inter*-residue dipolar connectivities and provide partial, site-specific assignments of  $^{13}\text{C}$  and  $^{15}\text{N}$  resonance signals. The secondary structure of the C-ter HsCen2/P17-XPC complex in a microcrystalline state appears similar to that found in solution. Conformational flexibility is probed through relaxation-compensated measurements of dipolar order parameters that exploit the dynamics of cross-polarization in multidimensional experiments. The extracted dipolar coupling constants and relevant order parameters reveal increased backbone flexibility of the loops except for residues involved in coordination with the  $\text{Ca}^{2+}$  cation that stabilizes the hydrophobic pocket containing the peptide P17-XPC.



## 1. INTRODUCTION

Human centrin 2 (HsCen2) is involved in the nucleotide excision repair (NER) process, as a subunit of a heterotrimer that includes the Xeroderma pigmentosum group C (XPC) and hHR23B proteins.<sup>1</sup> The interaction between HsCen2 and XPC plays a direct stimulatory role in the NER process by enhancing the specific binding of the heterotrimer (HsCen2/XPC/hHR23B) to damaged DNA.<sup>2</sup> The structure determination of the full centrin is hampered by its high flexibility and the tendency to self-associate.<sup>3</sup> On the other hand, by considering protein constructs of limited domains of HsCen2, it was possible to determine by liquid-state NMR the structure of the N-terminal domain (N-ter HsCen2: M1-S98)<sup>4</sup> and of its C-terminal domain (C-ter HsCen2: T94-Y172).<sup>5</sup> Later studies showed the high affinity of the full HsCen2 binding site for a C-terminal 17-residue fragment of XPC (<sup>847</sup>NWKLLAKGLLIR-ERLKR<sup>863</sup>), henceforth called P17-XPC.<sup>6</sup> Finally, target peptides<sup>2</sup> were used to show that, in the presence of  $\text{Ca}^{2+}$ , the binding affinity of P17-XPC to HsCen2 is essentially governed by the C-terminal domain of the protein. The  $\text{Ca}^{2+}$

dependent structural features of the overexpressed C-terminal domain of HsCen2 and the target peptide (C-ter HsCen2/P17-XPC complex) were also studied by liquid-state NMR and by molecular dynamics.<sup>7</sup> The C-ter HsCen2/P17-XPC complex adopts the conformation of a classical  $\text{Ca}^{2+}$  saturated EF-hand domain ( $\alpha$ -helix-loop- $\alpha$ -helix) with two EF-hand motifs (EF-III and EF-IV) separated by a linker loop.<sup>8</sup> The complex acquires a unique 3D structure in the presence of an excess of calcium and a 1:2 stoichiometric ratio C-ter HsCen2:P17-XPC. The EF-hand loops III and IV adopt an open conformation, creating a deep hydrophobic cavity that can bind the P17-XPC peptide.

Recent advances in magic-angle spinning (MAS) solid-state NMR spectroscopy have enabled detailed investigations at atomic resolution of protein structure, function, and dynamics.<sup>9</sup> Furthermore, solid-state NMR has also been used for mapping protein–protein interactions and rearrangements upon binding

**Received:** October 8, 2012

**Revised:** November 22, 2012

**Published:** November 28, 2012

revealed by site-resolved chemical shift perturbations as in the case of site-specific structural rearrangements of a scorpion toxin in the presence of a  $K^+$  channel analogue.<sup>10</sup> In this specific case, the sample of inhibitor toxin-membrane protein complex was in the form of pelleted proteoliposomes. Chemical shift changes of specific residues that map the complexation region of the periplasmic disulfide-donor enzyme DsbA covalently bound to its oxidizing agent DsbB as a pellet have also been studied by solid-state NMR.<sup>11</sup>

Solid-state NMR investigations of centrins or their complexes with target peptides have not been reported so far. The main purpose of the present work is to record reliable information about structural and motional features of the U- $(^{13}\text{C}, ^{15}\text{N})$ -[C-ter HsCen2]/P17-XPC complex in microcrystalline forms. For this, we combined a number of complementary multidimensional solid-state NMR techniques based on dipolar heteronuclear interactions. Some experiments were used for the first time in the study of microcrystalline proteins. More particularly, in the first part, we discuss how the experimental conditions and procedures of sample crystallization determine the quality of solid-state NMR spectra and the internal mobility of backbone and side-chain sites of the complex. In the second part, we take advantage of a dipolar recoupling sequence for obtaining partial site-specific assignments of  $^{13}\text{C}$  and  $^{15}\text{N}$  isotropic chemical shifts, especially of the EF-III, EF-IV, and linker loops that stabilize, in the presence of  $\text{Ca}^{2+}$  cation, the hydrophobic pocket containing the peptide P17-XPC. Finally, we exploit an approach for probing conformational flexibility through relaxation-compensated measurements of dipolar order parameters.

## 2. EXPERIMENTAL SECTION

Protein expression and purification protocols and the preparation of solutions of the complex are described in Supporting Information.

**Preparation of Microcrystals.** The precipitating agent was composed of 42% PEG 600 in 0.2 M imidazole malate at pH 5.4. We observed two different types of crystalline entities: *sea-urchin-like* crystals which are clusters of very thin needles and *plate-like* crystals which have larger widths and lengths than sea-urchin-like crystals and larger volume/surface ratios.<sup>12</sup> Sea-urchin-like crystals (sample A, Figure 1A) were obtained by the sitting-drop vapor diffusion method at 277 K by mixing 1–20  $\mu\text{L}$  of the stock solution of the complex with an equivalent volume of precipitating agent.

Each reservoir well contained 700  $\mu\text{L}$  of precipitating agent. Sea-urchin-like crystals appeared after 24 h, and the crystals were harvested after 2 days. The crystallization yield is estimated to 50% by measuring the optical density of the supernatant at 280 nm and to 80% by measuring the optical density at 280 nm of crystals dissolved in a 6 M guanidinium hydrochloride solution. Subsequently, about 15 mg of the microcrystals were used to fill a 2.5 mm rotor. The filling of the rotors was carried out by ultracentrifugation with home-built adaptors similar to those described in the literature.<sup>13</sup> A sample containing only plate-like crystals (sample B, Figure 1B) was obtained by the batch method by mixing equal volumes (2–50  $\mu\text{L}$ ) of the stock solution of the complex and the precipitating agent on a cell-culture plate. The plate was then refrigerated to 277 K. Plate-like crystals appear after 1 day, and the crystals were collected after 3 days. The crystallization yields are similar for plate-like and for sea-urchin-like crystals. Part of the plates thus obtained were used to fill a 2.5 mm rotor.

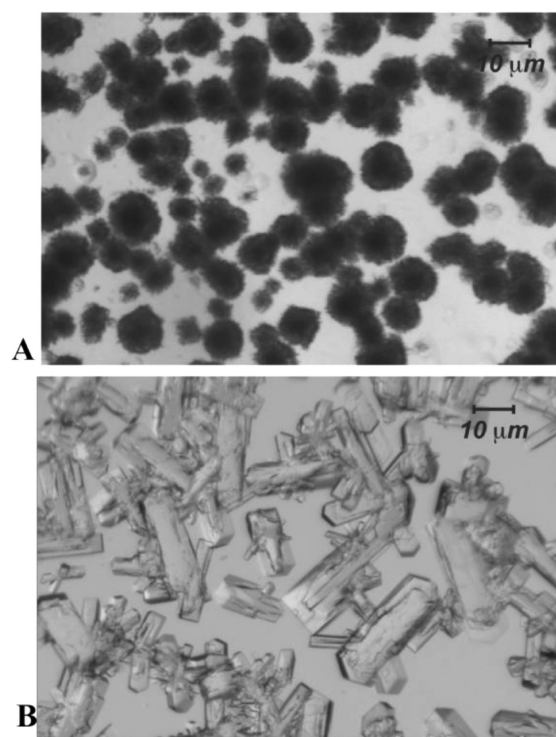


**Figure 1.** Microcrystalline forms of the C-ter HsCen2/P17-XPC complex. (A) Sea-urchin-like crystals grown by the sitting-drop vapor diffusion method at 277 K. (B) Plate-like crystals obtained with a macro-scaled batch method at 277 K. All pictures were photographed at 60 $\times$  magnification.

**NMR Experiments and Numerical Simulations.** All experiments were performed at  $T = 271$  K on a Bruker Avance II spectrometer with a 2.5 mm rotor spinning at a frequency  $\nu_r = 10$  kHz in a magnetic field of 9.4 T (400 MHz for  $^1\text{H}$ ). The  $^{13}\text{C}$  chemical shifts were referenced with respect to the carboxyl carbon of  $\alpha$ -glycine ( $\delta_{\text{iso}} = 176.5$  ppm).<sup>14</sup> The pulse sequences used in this work are shown in the Supporting Information. A one-dimensional version of the cross-polarization inversion (CPI) pulse sequence<sup>15,16</sup> was used for a rough visualization of the relative molecular mobility of different parts of the protein in different samples. The constant-time TORQUE pulse sequence<sup>17</sup> was used in two- and three-dimensional experiments to determine the heteronuclear dipolar couplings and the relevant order parameters while quenching the dependence on the proton  $T_{1\rho}$ .<sup>17,18</sup> The phase-alternated recoupling irradiation scheme PARIS (with recoupling condition  $N = 1/2$ )<sup>19</sup> was exploited in 2D  $^{13}\text{C}$ – $^{13}\text{C}$  and  $^{15}\text{N}$ – $^{15}\text{N}$  correlation experiments. Heteronuclear PISSARRO decoupling,<sup>20</sup> a supercycled version of the phase-alternated (XiX) decoupling scheme,<sup>21</sup> was applied during both evolution and detection intervals in all experiments. Numerical simulations were carried out with SPINE-VOLUTION<sup>22</sup> or by using an exact analytical treatment of isolated spin pairs under MAS including spin diffusion effects.<sup>23</sup>

## 3. RESULTS AND DISCUSSION

**3.1. Spectral Features for Various Crystallization Conditions.** The spectral resolution of solid-state NMR spectra of proteins depends on the experimental conditions and procedures of sample precipitation or crystallization.<sup>24–27</sup> The relationship between the crystal quality or the crystalline form of the protein and the observed line widths of the

resonance signals remains to be clarified. Variations of chemical shifts between different microcrystalline preparations and between solid- and liquid-state NMR spectra have also been reported in ubiquitin<sup>28</sup> and recently related to local differences in dynamics and conformation.<sup>29</sup> As discussed above, different experimental conditions and procedures may be used for obtaining microcrystalline samples of the C-ter HsCen2/P17-XPC complex, in particular sea-urchin-like crystals (sample A) and plate-like crystals (sample B). While the standard  $^{13}\text{C}$  CP-MAS spectra of both samples show very similar resonance signals in the carboxyl and aromatic regions, the aliphatic regions reveal significant differences, especially in the  $\text{C}\alpha$  region (50–62 ppm) and in some  $\text{CH}$  or  $\text{CH}_2$  groups of side-chains (25–42 ppm) (Figure 2, top). To get some insight into the

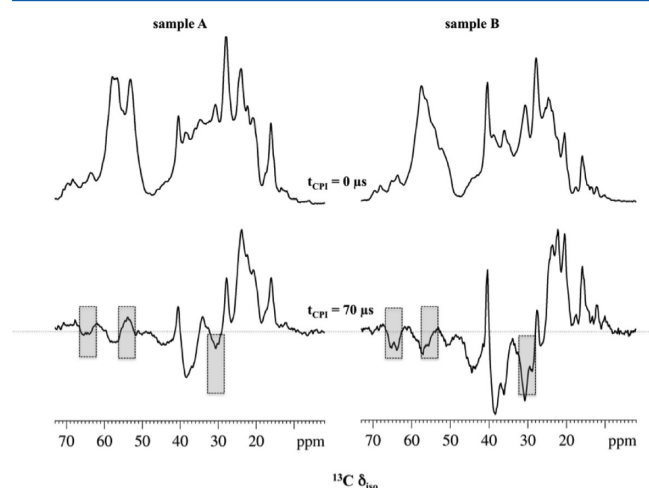


**Figure 2.** Expansions of the aliphatic regions of  $^{13}\text{C}$  spectra of samples A and B recorded with cross-polarization (top) and cross-polarization inversion (bottom). In all cases, a 300  $\mu\text{s}$  cross-polarization contact time was used while the cross-polarization inversion spectra were recorded after an additional phase-inverted rf irradiation of 70  $\mu\text{s}$  duration. All spectra were recorded in a magnetic field of 9.4 T (400 MHz for  $^1\text{H}$ ) with a spinning frequency of 10 kHz.

origins of these differences, which may result from variations in chemical shifts and from local differences in dynamics, we recorded the  $^{13}\text{C}$  spectra of both samples with the CPI pulse sequence which can be used for selective inversion or suppression of resonance signals depending on the proton–carbon dipolar couplings which in turn are governed by local dynamics.<sup>30</sup> A short interval  $t_{\text{CPI}}$  after cross-polarization leads to selective inversion for the most rigid  $\text{CH}$  and  $\text{CH}_2$  groups, while the resonance signals of more mobile sites, including  $\text{CH}_3$  groups, will maintain their positive intensity. This is visualized in the CPI spectra shown in Figure 2 (bottom) where all methyl resonances (9–25 ppm) have positive intensities for both samples. The same occurs for a resonance signal around 40 ppm, assigned (*vide infra*) to the side-chain  $\text{CH}_2(\epsilon)$  carbons in lysine residues that are endowed with substantial mobility. More interestingly, striking differences in the intensities highlighted by shaded boxes in Figure 2 suggest substantial differences in molecular mobility.

This is clearly the case for a region between 29 and 33 ppm dominated by resonance signals of the  $\text{C}\beta$  carbons from lysine, valine, and aspartic acid residues (*vide infra*) showing much stronger negative intensities reflecting higher rigidity of these sites in sample B than in sample A. Similar fingerprints of increased molecular mobility in sample A are visible for the  $\text{C}\alpha$  resonance signals between 52 and 58 ppm, showing positive and negative intensities respectively for samples A and B as well as for the serine and threonine  $\text{C}\beta$  resonances around 62–69 ppm which are either suppressed or inverted.

Further evidence that corroborates increased overall mobility of  $\text{C}\alpha$  carbons in sample A comes from the dipolar coupling constant  $D_{\text{CH}}^{\text{exp}}$  extracted from relaxation-compensated cross-polarization dynamics measurements (the TORQUE pulse sequence, see part 3.3). This leads to substantially smaller C–H dipolar splittings of the  $\text{C}\alpha$  carbons in sample A, as shown in Figure 3.

Moreover, significantly different spectroscopic fingerprints of samples A and B are revealed by the 2D  $^{13}\text{C}$ – $^{13}\text{C}$  correlation spectra shown in Figure 4 where the observed cross-peak amplitudes reveal strongly reduced polarization transfer efficiency in sample A. This again proves a higher molecular

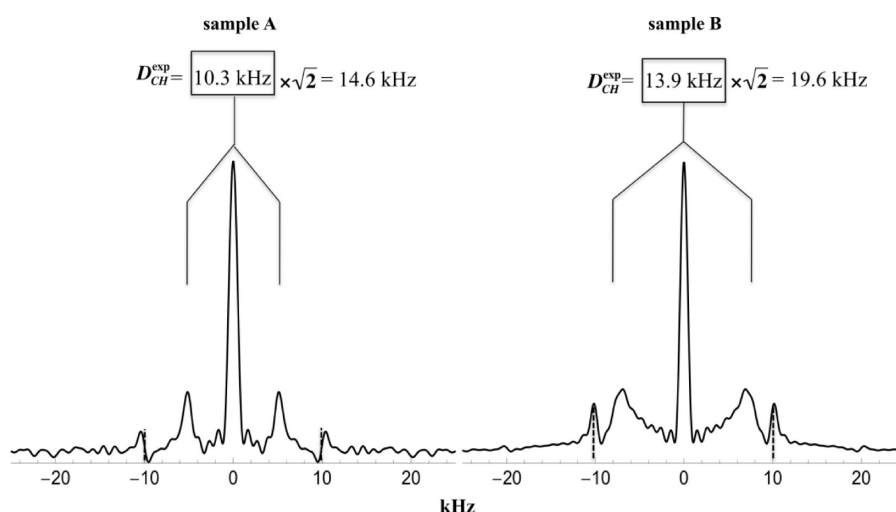


**Figure 3.** Experimental dipolar spectra of the  $\text{C}\alpha$  carbons (resonance signals between 50 and 62 ppm) of samples A and B recorded by relaxation-compensated cross-polarization measurements at  $\nu_r = 10$  kHz (TORQUE experiments with a total constant spin-lock time of 1 ms). Vertical dotted lines indicate the positions of narrow lines at integral multiples of the spinning frequency. The dipolar coupling constant  $D_{\text{CH}}^{\text{exp}}$  is extracted by multiplying the dipolar splitting by a factor of  $\sqrt{2}$  to account for the  $n = -1$  cross-polarization matching condition.



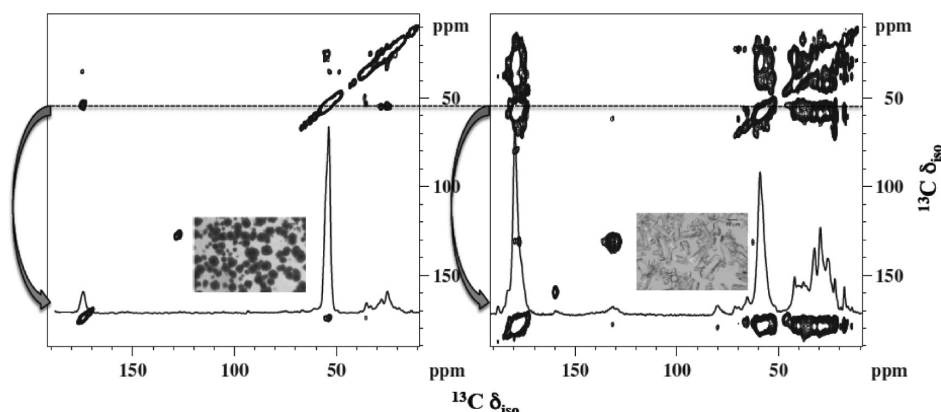


**Figure 4.**  $^{13}\text{C}$ – $^{13}\text{C}$  correlation spectra of sample A (left) and sample B (right) recorded on a 400 MHz spectrometer by using PARIS recoupling with a proton rf amplitude  $\nu_{\text{H}} = 15$  kHz during a mixing time of 50 ms. The 2.5 mm rotors were spun in both cases at 10 kHz. Both spectra were recorded with 64 and 1024 points in the F1 and F2, respectively, zero-filled to 4 k before Fourier transformation, and processed with a cosine bell function in both dimensions. Note that the intensities of the cross-peaks in a cross-section at 56.4 ppm corresponding to  $\text{C}^{\alpha}$  carbons from the  $\alpha$ -helix show much higher polarization transfer efficiency in sample B.

mobility and possibly a higher structural disorder of the protein in this sample associated with its specific crystal morphology.

The fingerprints of different internal mobilities of the protein in samples A and B discussed above could be related to a striking difference in the  $^1\text{H}$  spectra of water molecules. In agreement with earlier reports on different types of water molecules in protein samples,<sup>13,31</sup> we observed (Figure S2, Supporting Information) two distinct proton signals with isotropic chemical shifts close to 4.7 and 5.0 ppm and that we ascribe, respectively, to (i) bulk (supernatant) water and water molecules located on the surface of the protein that are engaged in fast exchange with bulk water and (ii) tightly bound water located either within crystallites or directly surrounding them (crystal water). As expected, crystal water has a faster  $T_1$  relaxation than the bulk/surface water (see the Supporting Information). More interestingly, dramatic differences in the intensities of these two signals appear in both spectra. While the signal of the bulk/surface water largely dominates in sample A, the opposite scenario is seen in sample B where mainly crystal water is observed. This could explain a higher internal mobility and possibly higher structural disorder of the protein in sample A.

Finally, in contrast to the  $^{13}\text{C}$  spectra, the  $^{15}\text{N}$  spectra (Figure 5) of the backbone resonances of sample B reveal higher spectral resolution over a range of temperatures between 236 and 273 K. This strongly suggests the presence of higher structural homogeneity (local order) in this sample. Standard one-dimensional  $^{15}\text{N}$  CP-MAS spectra seem to be more sensitive to this distinction than  $^{13}\text{C}$  spectra, probably due to the higher sensitivity of  $^{15}\text{N}$  chemical shifts to the hydrogen bonding network.

In summary, it appears that the observed differences in the heteronuclear dipolar coupling constants, the efficiency of polarization exchange, and the spectral resolution are related to the experimental conditions and procedures of sample precipitation and/or crystallization which may affect the internal mobility of the protein and determine the quality of solid-state NMR spectra of hydrated crystalline proteins. Further spectroscopic and crystallographic studies will be necessary to better understand the structural origins of the observed differences that are possibly related to the presence of different crystalline forms or polymorphs as to crystal imperfections.

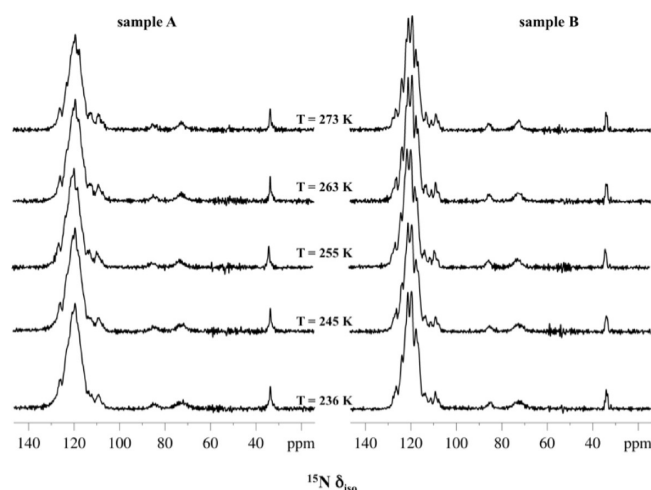


**Figure 5.**  $^{15}\text{N}$  CP-MAS spectra of samples A and B recorded at different temperatures on a 400 MHz spectrometer with a spinning frequency of 10 kHz and a cross-polarization contact time of 150  $\mu\text{s}$ .

**3.2. Partial Site-Specific Assignments of  $^{13}\text{C}$  and  $^{15}\text{N}$  Resonances.** Two-dimensional homonuclear correlation spectroscopy provides a powerful tool for the determination of spectral connectivities and for the assignment of resonance lines. Efficient magnetization transfer between spins  $S$  such as carbon-13 or nitrogen-15 is a prerequisite for the assignment of solid-state NMR spectra of isotopically enriched molecules in biosolids. Here we exploit 2D dipolar  $^{13}\text{C}$ – $^{13}\text{C}$  and  $^{15}\text{N}$ – $^{15}\text{N}$  correlation experiments to reveal *intra*- and *inter*-residue connectivities and assign the resonance signals. We used the basic PARIS ( $N = 1/2$ ) sequence<sup>19</sup> which allows one to achieve an efficient exchange of magnetization with moderate rf-field recoupling amplitudes. The efficiency of PARIS recoupling does not depend on the rf amplitude<sup>19,32</sup> which need not be matched to the spinning frequency. PARIS is also largely immune to the inhomogeneity of the rf field,<sup>19</sup> so that the full sample volume effectively contributes to the signal whatever the spinning frequency. Very recently, we used the PARIS approach to record sensitive 2D correlation spectra of a microcrystalline protein,<sup>32</sup> amyloid fibrils,<sup>33</sup> and mixtures of crystallographic forms<sup>34</sup> and to restore the symmetry in 2D correlation experiments.<sup>35</sup> All experiments presented in this part were

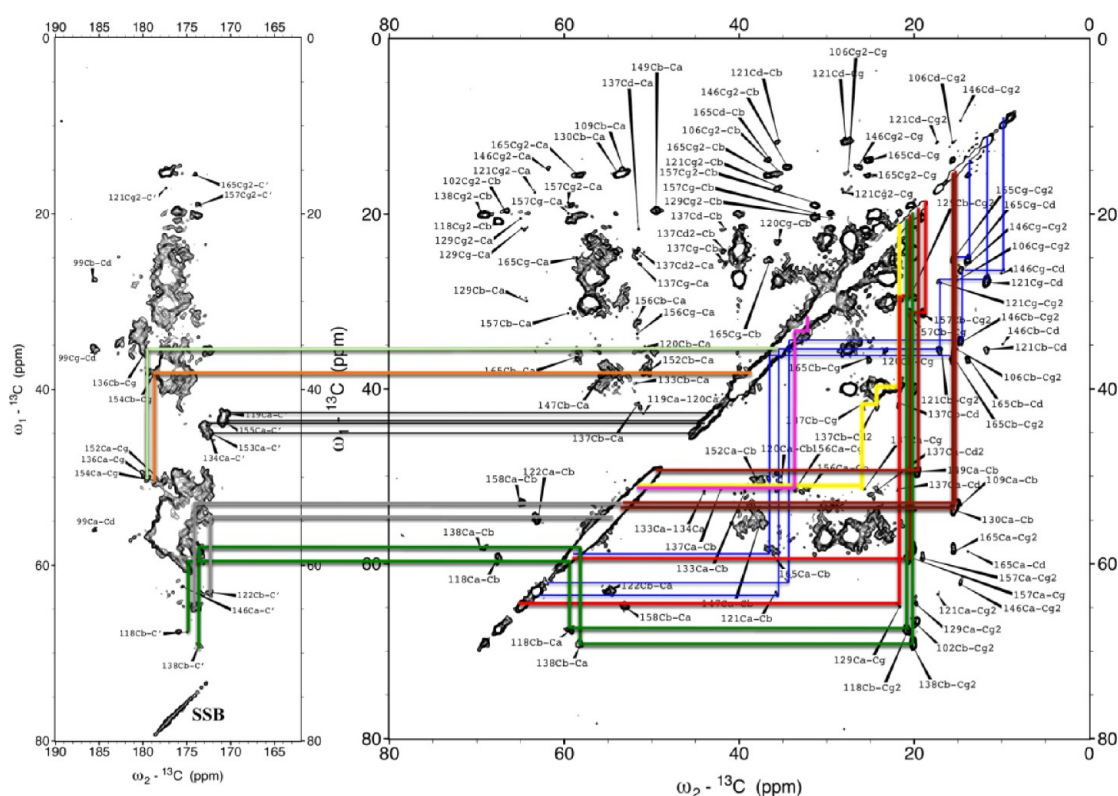


**Figure 6.** PARIS  $^{13}\text{C}$ – $^{13}\text{C}$  correlation spectrum of the C-ter HsCen2/P17-XPC complex recorded in a 9.4 T magnetic field with a mixing time of  $\tau_m = 20$  ms and an rf recoupling amplitude of  $\nu_{\text{IH}} = 15$  kHz. The 2.5 mm rotor was spun at  $\nu_r = 10$  kHz. The intraresidue pathways and assignments of selected spin systems are drawn in color as follows: isoleucine, blue; valine, red; alanine, brown; leucine, yellow; aspartate, orange; asparagine, light green; glutamate, magenta; glycine, black; serine, gray; threonine, green.

run with sample B. The assignment procedure of the site-resolved  $^{13}\text{C}$  and  $^{15}\text{N}$  resonances in the solid state is based on liquid-state NMR data.<sup>7</sup>

**2D  $^{13}\text{C}$ – $^{13}\text{C}$  Correlation Experiments.** A two-step strategy was used for the assignment of  $^{13}\text{C}$  resonance signals. First, using a short mixing time of  $\tau_m = 20$  ms, the intraresidue connectivity paths of the spin systems of several amino acids like Ile, Val, Thr, Ser, Ala, Leu, or Gly were identified. Next, the inter-residue contacts between carbons of previously assigned amino acid spin systems  $i$  and  $i \pm 1$  were determined and assigned on the basis of correlation experiments recorded with longer mixing times ( $\tau_m = 50$  and 100 ms). Figure 6 shows a  $^{13}\text{C}$ – $^{13}\text{C}$  correlation spectrum recorded with a short mixing time which reveals characteristic chemical shift patterns of unambiguously identified isoleucines I106, I121, I146, and I165, valines V129 and V157, alanines A109, A130, and A149, phenylalanines F123 and F162, glycines G119, G134, G153, and G155, serines S122 and S158, and threonines T102, T118, and T138. In all cases, one-, two-, and three-bond correlations were drawn. Besides these well identified spin systems, two correlation pathways were found starting with leucine L133 in the linker loop and with glutamic acid E156 in the EF-IV loop.

A  $^{13}\text{C}$ – $^{13}\text{C}$  PARIS correlation spectrum recorded with a mixing time of 50 ms is shown in Figure 7. This helps to complete some intraresidue connectivity pathways of I121 and I146, thus leading to complete  $\text{C}'\text{-C}\alpha\text{-C}\beta\text{-C}\gamma_1\text{-C}\gamma_2\text{-C}\delta$  pathways. Interestingly, the cross sections (not shown) reveal a long-range cross-peak  $\text{CH}_3\delta\text{-C}'$  of I121 in the EF-III loop with a stronger intensity than the analogous cross-peak of I146 in the  $\alpha$ -helix. This might be ascribed to a higher structural

homogeneity of the I121 side-chain due to the presence of a hydrophobic interaction with the target peptide P17-XPC.<sup>36</sup>

Moreover, three inter-residue cross-peaks from sequential contacts (emphasized by dotted lines) involving glycines in the EF-hand loop IV (D154Ca–G155C' and E156Ca–G155C') and in the linker loop (L133Ca–G134Ca) show up in this spectrum. Other inter-residual contacts become apparent if the duration of the mixing time is equal to 100 ms (not shown).

The list of  $^{13}\text{C}$  resonances with assigned isotropic chemical shifts is given in Table 1 of the Supporting Information. The location of the assigned amino acids in the secondary structure of C-ter HsCen2/P17-XPC is depicted in Figure 8 which reveals that many of the unassigned resonances are located in the nonstructured N-terminal (residues 94–100) and C-terminal (residues 168–172) regions. This is analogous to earlier liquid-state NMR studies<sup>5,7</sup> where a similar lack of cross-peaks from the two terminal domains was attributed to the enhanced flexibility induced by conformational exchange on a  $\mu\text{s}$  time scale.

On the other hand, the extremely crowded spectral regions involving carbons from  $\alpha$ -helices make their unambiguous assignment difficult. This is especially true for the most abundant amino acids in the  $\alpha$ -helices which include seven lysines, eight glutamic acids, and six leucines. Chemical shift correlation plots between assigned resonances in solid- and liquid-state spectra<sup>7</sup> are shown in Figure 9.

Although some differences are expected between liquid- and solid-state spectra, possibly due to changes in the conditions of sample preparation, crystal contacts, nearby solvent molecules, and the protonation state at different pH values of the liquid sample and the mother solution of the crystallization, many

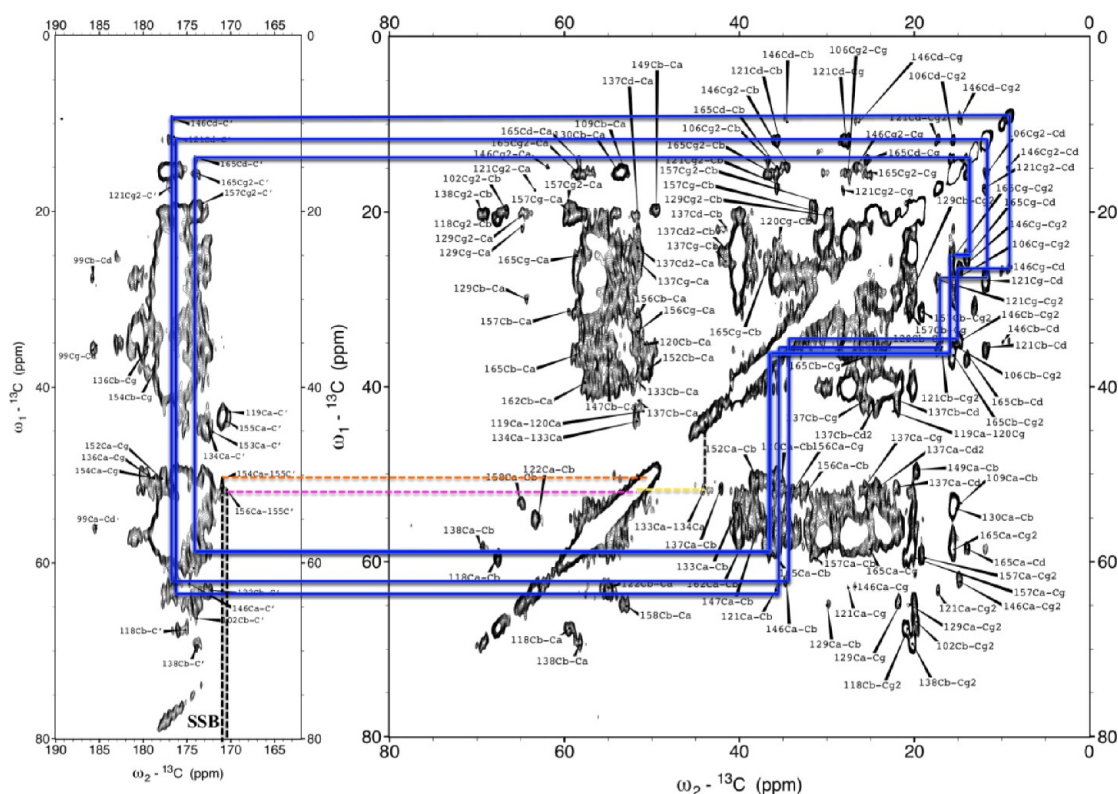


**Figure 7.** PARIS  $^{13}\text{C}$ – $^{13}\text{C}$  correlation spectrum of the C-ter HsCen2/P17-XPC complex recorded in 9.4 T with a mixing time of  $\tau_m = 50$  ms and an rf recoupling amplitude of  $\nu_{\text{IH}} = 15$  kHz. The 2.5 mm rotor was spun at  $\nu_r = 10$  kHz. Full intraresidue  $\text{C}'\text{-Ca-C}\beta\text{-C}\gamma_1\text{-C}\gamma_2\text{-C}\delta$  correlation pathways (continuous lines) are emphasized by continuous blue lines for I121, I146, and I163. The inter-residue correlations involving the cross-peaks D154Ca–G155C', E156Ca–G155C', and L133Ca–G134Ca are highlighted by dashed lines.

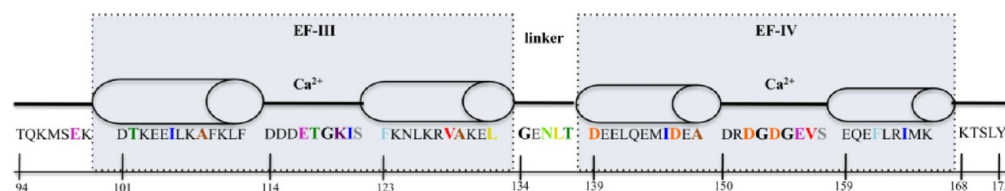


**Figure 8.** Secondary structure and amino acid sequence of the C-ter HsCen2/P17-XPC complex. The EF-hand III consists of residues between D101 and L133, while the EF-hand IV comprises residues D139–K167. The residues with assigned solid-state NMR  $^{13}\text{C}$  resonances are highlighted in bold with the same color code as in Figures 6 and 7.

resonances show very similar values in both sets of data. The best agreement is observed for the  $\text{Ca}$  and  $\text{C}\beta$  carbons which are very sensitive to the conformation. This strongly suggests that the secondary structure of the C-ter HsCen2/P17-XPC complex is indeed very similar in solution and microcrystalline states.

**$2\text{D } ^{15}\text{N}$ – $^{15}\text{N}$  Correlation Experiment.** Figure 10 shows the  $^{15}\text{N}$ – $^{15}\text{N}$  correlation spectrum of the C-ter HsCen2/P17-XPC complex. To get insight into the cross-peaks close to the diagonal, two spectra are overlaid showing data of the same experiment processed in two different ways. The  $^{15}\text{N}$  cross-peaks that are farthest from the diagonal were assigned in the spectrum processed using a standard exponential multiplication. The resolution enhancement of the cross-peaks located close to the diagonal was achieved by a Lorentzian-to-Gaussian apodization.

The assignments in the  $^{15}\text{N}$ – $^{15}\text{N}$  spectrum were based on chemical shifts in solution<sup>7</sup> starting with three identified backbone nitrogen signals of T118, G134, and R151 residues located, respectively, in the EF-III, linker, and EF-IV loops. In

particular, connectivities involving residue T118 range from D114 to I121 in the backbone sequence  $^{114}\text{DDDE}^{118}\text{TGKI}^{121}\text{I}$ , with the G134 resonance permitting the assignment of the  $^{134}\text{GENLTDE}^{141}\text{E}$  fragment and the R151 offering a starting point for the  $^{151}\text{RDGDGEVSEQEF}^{163}\text{L}$  pathway. Interestingly, most of the cross-peaks in the last sequence appear relatively far from the diagonal, thus revealing a particular shielding environment of the EF-IV loop. The list of isotropic chemical shifts of all assigned  $^{15}\text{N}$  resonances is given in Table 2 of the Supporting Information. The comparison of the isotropic chemical shifts in solution and in the microcrystalline state is shown in Figure 11.

As expected, larger variations are observed for the  $^{15}\text{N}$  chemical shifts than for the  $\text{Ca}$  and  $\text{C}\beta$  carbons. This must result not only from a stronger dependence of nitrogen shifts on hydrogen bonding and on electrostatic effects but also from the fact that the largest variations are observed within the loops which can differ significantly in their conformations in the liquid and solid state.



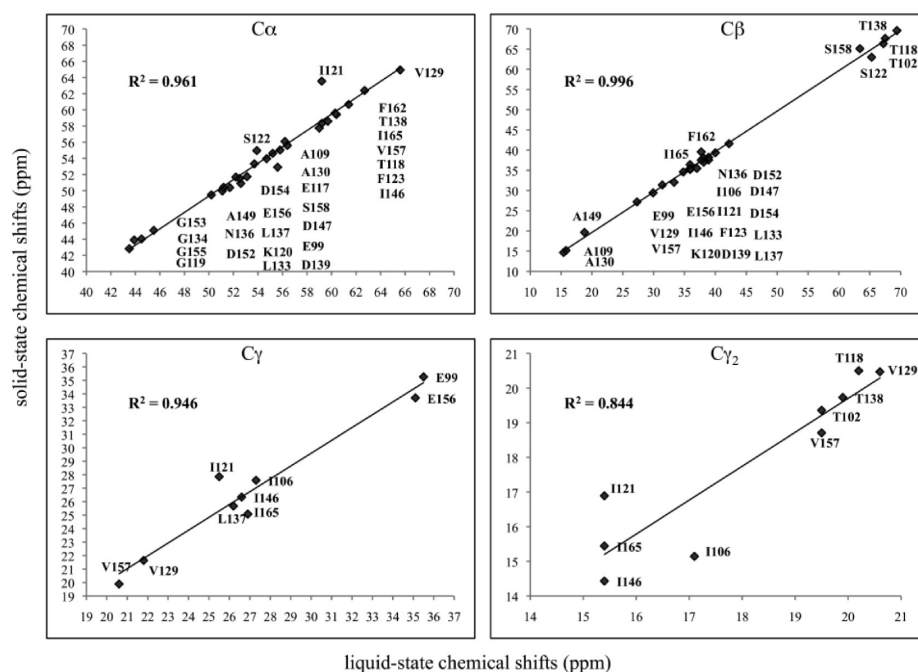


**Figure 9.**  $^{13}\text{C}$  chemical shift correlation plots between resonances assigned in the solid state (present work) and solution NMR data<sup>7</sup> for C-ter HsCen2/P17-XPC.

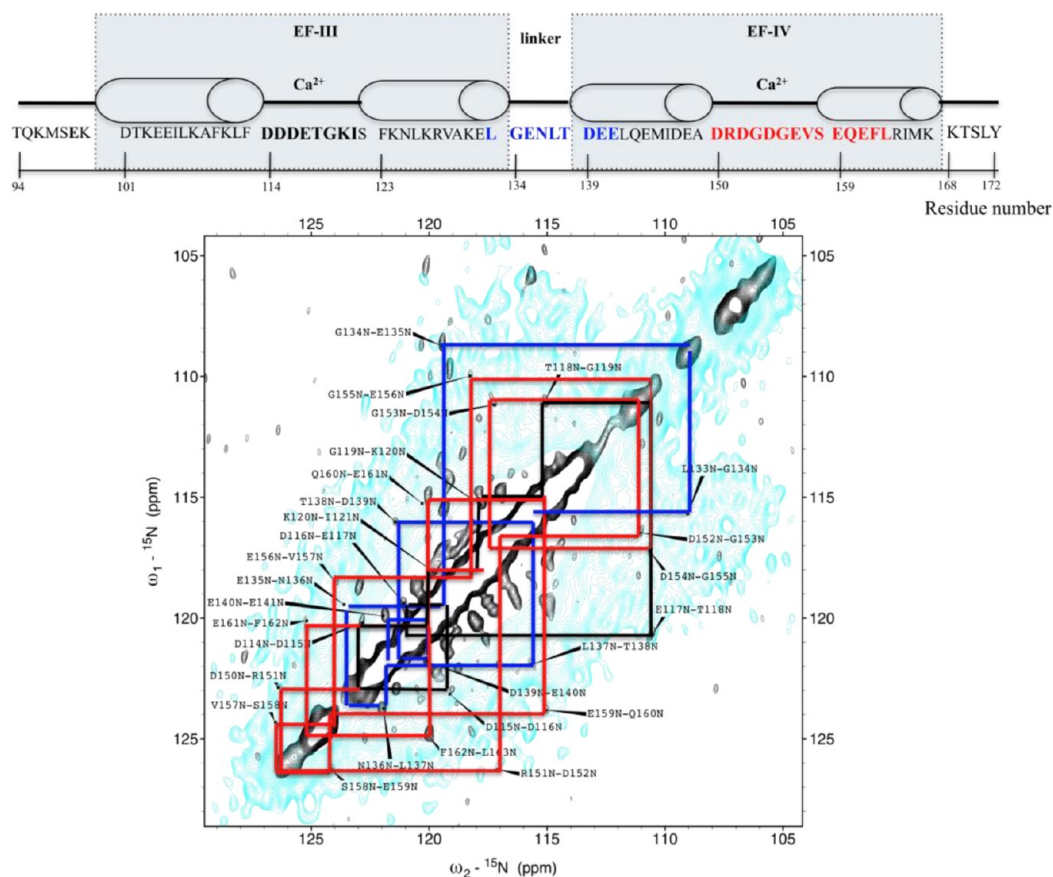


**Figure 10.** (bottom) PARIS  $^{15}\text{N}$ - $^{15}\text{N}$  correlation spectrum of the C-ter HsCen2/P17-XPC complex recorded in 9.4 T with a mixing time of  $\tau_m = 2$  s and an rf recoupling amplitude of  $\nu_{\text{IH}} = 15$  kHz. The 2.5 mm rotor was spun at  $\nu_r = 10$  kHz. The figure shows the overlay of two spectra processed with two different apodization functions: (cyan) spectrum apodized with a standard exponential multiplication using a line broadening of 5 Hz in both dimensions; (black) spectrum processed by using a Lorentzian-to-Gaussian apodization in F1 and F2. Sequential assignments coming mainly from the EF-III loop, the linker loop, and the EF-IV loop are highlighted with bold red dashed lines, black dash-dotted lines, and blue solid lines, respectively. The same color code is used in the scheme of the assigned amino acids of each region (top).

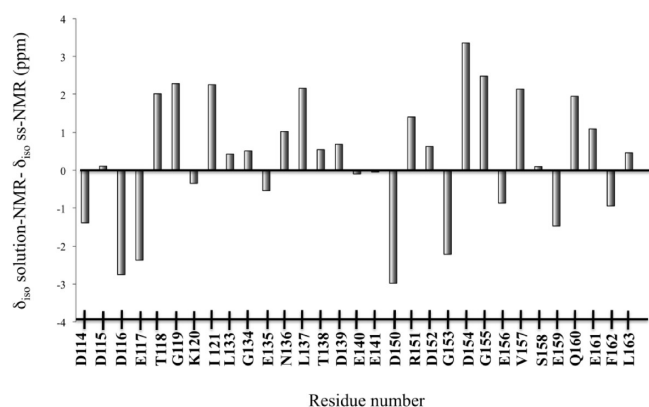


**Figure 11.** Comparison between the  $^{15}\text{N}$  isotropic chemical shifts of C-ter HsCen2/P17-XPC in solution<sup>7</sup> and in the solid state. The mean standard deviation is  $0.46 \pm 1.64$  ppm.

**3.3. Conformational Flexibility: Relaxation-Compensated Measurements of Dipolar Order Parameters.** The structure and dynamics are the cornerstones of the understanding of the molecular basis of the biological function of proteins. Internal protein dynamics play an important role in molecular recognition, ligand binding, catalysis, folding, or proton transfer. Solid-state NMR relaxation measurements

allow one to access internal motions on a micro- to millisecond time scale that is believed to be relevant for many biological processes.

As discussed in part 3.1, cross-polarization inversion spectra permit one to recognize at a glance the overall differences in molecular mobility of functional groups or sites through the intensities of the relevant signals (also see Figure S4, Supporting Information). The extent of averaging of anisotropic interactions by fast internal motions is usually described in terms of fast-limit order parameters  $\langle S \rangle$  that provide a measure of the amplitude of motions occurring on time scales up to the inverse of the interaction size.<sup>37</sup> Here we will access the order parameter defined as

$$\langle S \rangle = D_{\text{XH}}^{\text{exp}} / D_{\text{XH}}^{\text{rigid}} \quad (1)$$

by comparing the experimentally determined heteronuclear dipolar coupling  $D_{\text{XH}}^{\text{exp}}$  and the rigid-limit value  $D_{\text{XH}}^{\text{rigid}}$  calculated for  $^{13}\text{C}-^1\text{H}$  and  $^{15}\text{N}-^1\text{H}$  bond lengths.

Several different approaches have been used to measure the motionally averaged dipolar couplings and relevant order parameters in proteins.<sup>29,38–42</sup> As demonstrated first on a single crystal of ferrocene,<sup>43</sup> the oscillatory build-up of the transfer of magnetization by cross-polarization<sup>44</sup> may be used to characterize the details of heteronuclear interactions in static solids. Experimental evidence was later presented showing that

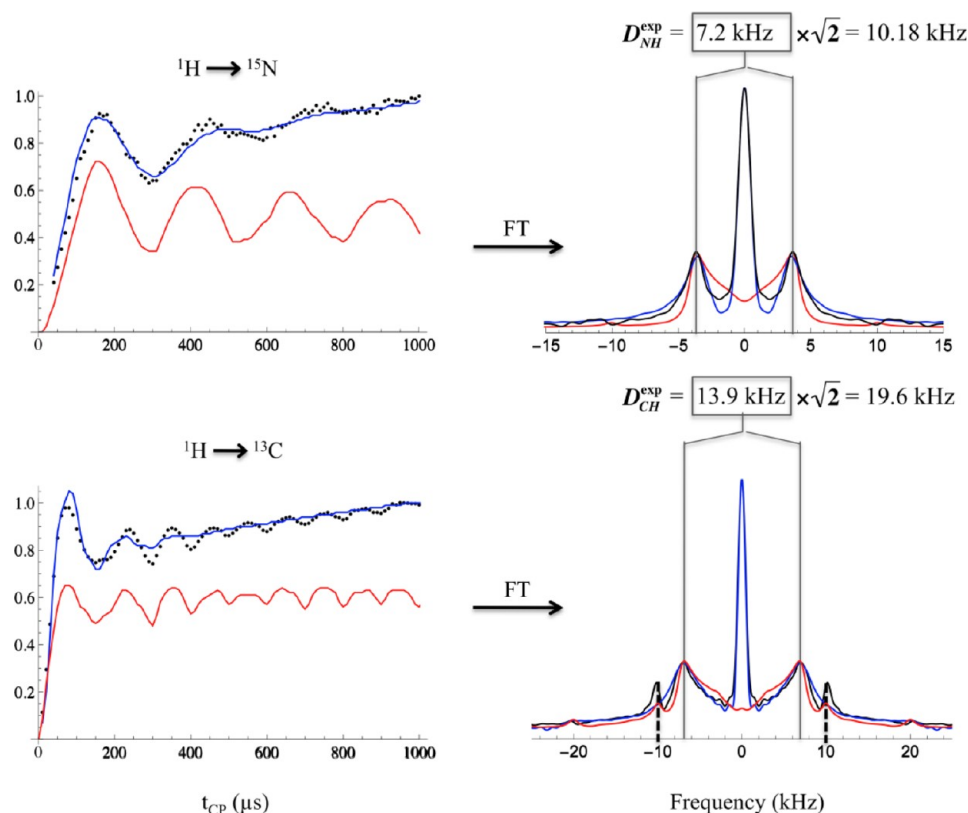


**Figure 12.** (left)  $^1\text{H} \rightarrow ^{13}\text{C}$  and  $^1\text{H} \rightarrow ^{15}\text{N}$  cross-polarization (CP) build-up plots recorded for the backbone  $\text{C}\alpha$  and NH resonances of the C-ter HsCen2/P17-XPC complex (sample B) in relaxation-compensated cross-polarization measurements at  $\nu_r = 10$  kHz (TORQUE with a constant spin-lock time of 1 ms) and  $T = 271$  K. (right) Experimental dipolar spectra (in black) obtained after Fourier transform (FT) of the build-up curves. Vertical dotted lines indicate the positions of narrow lines at integral multiples of the spinning frequency. The dipolar coupling constants  $D_{\text{CH}}^{\text{exp}}$  and  $D_{\text{NH}}^{\text{exp}}$  were extracted from the splittings multiplied by a factor of  $\sqrt{2}$  to account for the  $n = -1$  CP matching condition. Simulated build-up curves and corresponding dipolar spectra were obtained with the SPINEVOLUTION program<sup>21</sup> for isolated pairs of spins (in red), while the fitting of the experimental build-up curves and corresponding dipolar spectra (in blue) were obtained using the exact analytical treatment for isolated pairs of spins that includes spin diffusion effects<sup>23</sup> and implemented using the Scilab<sup>50</sup> software.



cross-polarization also offers a way of obtaining information about local dipolar fields in solids that are spinning about the magic angle<sup>15,45</sup> without applying any homonuclear dipolar decoupling. This permits one to circumvent the challenging problem of the precise determination of the heteronuclear scaling factor. Indeed, when using experimental schemes that include homonuclear decoupling methods like Lee–Goldburg cross-polarization (LG-CP),<sup>46</sup> special care must be taken to measure the heteronuclear scaling factor under the same experimental conditions during the dipolar evolution, and to control variations of the scaling factor over a range of frequency offsets.<sup>47</sup> Local-field measurements through regular cross-polarization dynamics take advantage of the coherent energy transfer in the initial periods of a few hundreds of microseconds where information on local heteronuclear interactions is revealed in solids where heteronuclear dipolar couplings are larger than homonuclear dipolar couplings. This situation is typical for protonated low-gamma nuclei. In contrast with the LG-CP approach, the regular CP experiments are not very sensitive to the carrier frequency due to the truncation of chemical shift terms by intense rf-fields. To compensate for harmful effects of proton  $T_{1\rho}$  relaxation that can hide subtle details of cross-polarization dynamics,<sup>17,18,48</sup> we used the TORQUE pulse sequence to quench the proton  $T_{1\rho}$  dependence.<sup>17</sup> As shown in Figure 12 (left) for the integrated intensities of signals of the backbone  $C\alpha$  and N–H regions, the relaxation-compensated cross-polarization dynamics immediately reveals two distinct features: an oscillating polarization transfer governed by one-bond dipolar C–H and N–H dipolar couplings, followed by an exponential growth due to the equilibration of the proton magnetization via spin-diffusion processes. The initial oscillations are characteristic of the largely coherent nature of the polarization transfer<sup>43</sup> in spin systems with moderate proton–proton couplings. Consequently, the Fourier transform of the time dependence leads to dipolar spectra (Figure 12, right) featuring modified Pake doublets due to the oscillating heteronuclear polarization transfer, while proton spin-diffusion leads to an isolated central peak.<sup>23,16,49</sup>

It is worth pointing out that the dipolar spectra shown in Figure 12 are largely dominated by the most rigid C–H and N–H pairs in the 44 residues of the four  $\alpha$ -helices which have larger splittings than the 23 residues of the two EF-hand loops and the central linker, while the terminal parts do not appear to contribute significantly. Further experimental evidence shows that the rf-field inhomogeneity has a negligible effect on the dipolar splittings at accurately determined  $n = \pm 1$  Hartmann–Hahn conditions (see Figure S5, Supporting Information, for a comparison of the lineshapes recorded with a fully packed rotor and with a small sample placed in the central part of the rotor). The extension of numerical simulations to a larger number of spins (Figure S6, Supporting Information) shows that the remote protons have only minor effects. This implies that, in contrast to the requirements of REDOR for measurements of dipolar order,<sup>42</sup> the use of highly deuterated samples is not mandatory. If one considers the rigid C–H and N–H bond lengths to be 1.102 and 1.02 Å, respectively, the order parameters calculated from eq 1 with experimentally determined dipolar couplings  $D_{CH}^{exp}$  and  $D_{NH}^{exp}$  are  $\langle S \rangle = 0.87 \pm 0.02$  and  $0.89 \pm 0.02$ . For a model of an X–H vector which freely diffuses within a cone,<sup>51</sup> and assuming that the reduced dipolar couplings do not result from an elongation of the X–H bonds due to hydrogen bonding, the half angles of the cone-opening estimated from these measured order parameters are

approximately  $\theta = 24 \pm 2^\circ$  and  $22 \pm 2^\circ$ . This would suggest a very similar conformational flexibility of C–H and N–H vectors in  $\alpha$ -helices if we assume the same model of internal motions for both types of bonds.

To probe the conformational flexibility of functional groups that lead to well-resolved cross-peaks, we exploited  $^{13}C$ – $^{13}C$  correlations for measuring dipolar oscillations during 3D TORQUE/exchange experiment (see pulse sequence in Figure S1d, Supporting Information). We checked that the same dipolar coupling constants were measured through dipolar oscillations of the cross-peaks and diagonal peaks (Figure S7, Supporting Information). Four representative dipolar spectra of C–H couplings of  $C\alpha$  and  $C\beta$  carbons are shown in Figure 13. A full set of extracted dipolar coupling constants and order parameters is shown in Figure 14.

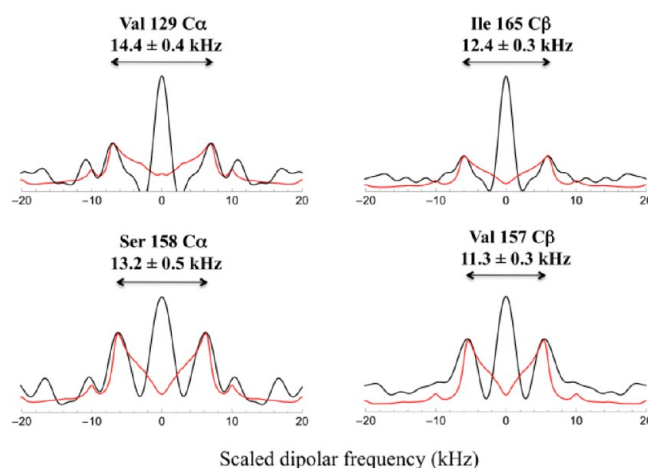


**Figure 13.** (Black) Experimental dipolar  $^1H$ – $^{13}C$  spectra of  $CH\alpha$  and  $CH\beta$  resonances of residues V129 and T102 in two different  $\alpha$ -helices and of S158 and V157 in the EF-hand IV loop of C-ter HsCen2/P17-XPC. (Red) Spectra simulated for an isolated spin pair. The dipolar splittings are scaled by a factor of  $1/\sqrt{2}$  due to the  $n = -1$  CP condition.

Most observable dipolar couplings stem from residues located in the EF-III, EF-IV, and linker loops and reveal an average carbon–proton dipolar coupling constant of about 17 kHz. This corresponds to an order parameter of  $\langle S \rangle = 0.76 \pm 0.05$ , while for the whole  $C\alpha$  region, which is dominated by  $\alpha$ -helix resonances, one obtains  $\langle S \rangle = 0.87 \pm 0.02$  (see above). Interestingly, the highest order parameter in the loops, apart from the  $CaH_2$  of glycines, is observed for the  $C\alpha$  ( $0.83 \pm 0.05$ ) and  $C\beta$  ( $0.98 \pm 0.02$ ) resonances of serine 158 as well as the  $C\beta$  ( $0.91 \pm 0.05$ ) resonance of serine 122. Both of these residues are involved in coordination of their hydroxyl groups and the  $Ca^{2+}$  cations that stabilize the hydrophobic pocket containing the P17-XPC peptide.<sup>7,36</sup> A somewhat enhanced flexibility is also observed for alanine 130 and 149 and isoleucines 146 that are in the second and third  $\alpha$ -helices. This appears to confirm earlier observations that these helices might not be completely structured.<sup>7,36</sup> Finally, the lowest order parameters  $0.5 < S < 0.6$  are observed for the  $C\gamma_1H_2$  resonances of isoleucine 106, 121, and 146 due to enhanced mobility of their side-chains. Combining site-specific dipolar order parameters with relaxation measurements and molecular dynamics should allow one to obtain deeper insight into the mobility of backbone and side-chains.

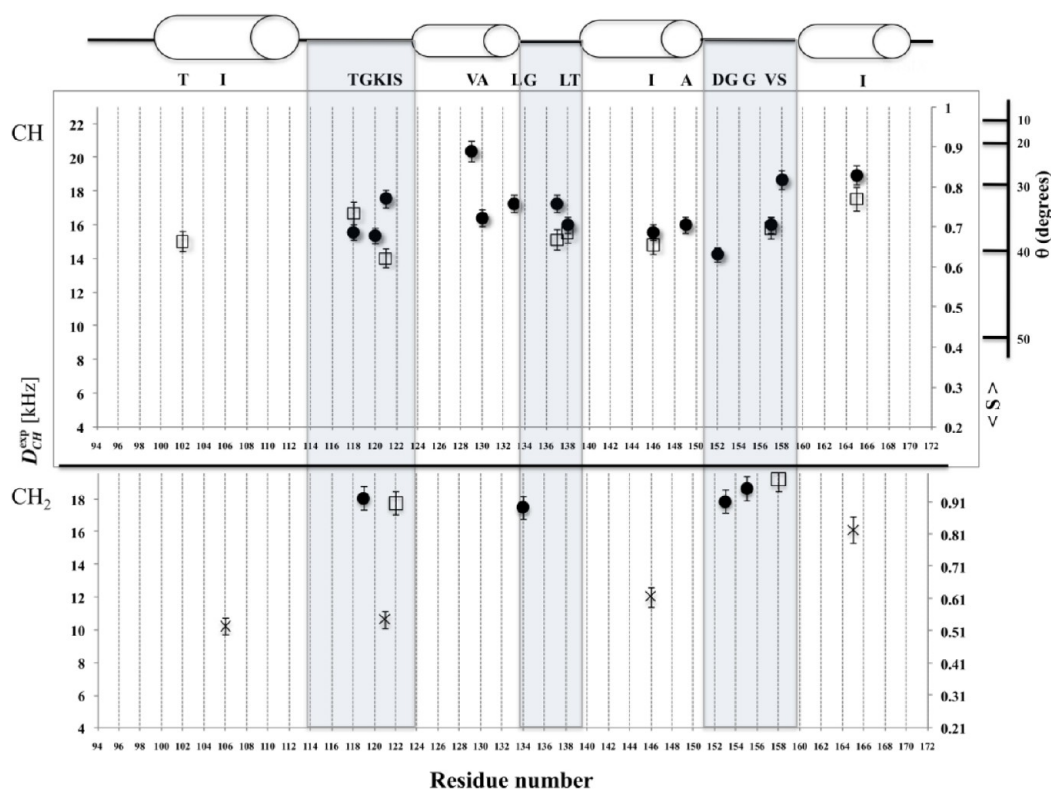


**Figure 14.** Experimental  $^1\text{H}$ – $^{13}\text{C}$  dipolar coupling constants ( $D_{\text{CH}}^{\text{CH}}$ ) for different residues in C-ter HsCen2/P17-XPC extracted from dipolar oscillations of well-resolved and unambiguously assigned cross-peaks in the  $^{13}\text{C}$ – $^{13}\text{C}$  correlation spectra. Filled circles, empty squares, and crosses represent  $\text{C}^\alpha$ ,  $\text{C}^\beta$ , and  $\text{C}^\gamma$  resonances, respectively. The order parameter  $\langle S \rangle$  was calculated assuming a C–H distance of 1.102 Å. The angle  $\theta$  refers to the half angle of the cone in which the C–H vector is assumed to diffuse freely.<sup>51</sup> In the case of  $\text{CH}_2$  groups, the dipolar splitting for a rigid spin system was obtained by numerical simulations including all homo- and heteronuclear interactions with the crystallographic atomic coordinates of L-glycine.

#### 4. CONCLUSIONS

Structural and motional features of the C-terminal part of the Human Centrin 2/P17-XPC complex in a microcrystalline form have been investigated by choosing complementary solid-state NMR methods. We have shown that different experimental conditions and procedures for sample crystallization determine the quality of solid-state NMR spectra and the internal mobility of the protein. Sensitive 2D dipolar  $^{13}\text{C}$ – $^{13}\text{C}$  and  $^{15}\text{N}$ – $^{15}\text{N}$  correlation spectra have been recorded using PARIS recoupling to reveal *intra*- and *inter*-residue connectivities and to assign resonance signals. There are some differences between the chemical shifts in the liquid and solid state that are probably due to variations in sample preparation and to differences in protonation (the liquid sample and the mother solution used for crystallization may have different pH values). By and large, however, many resonances appear at similar shifts in the liquid- and solid-state spectra. The best agreement is observed for the  $\text{C}\alpha$  and  $\text{C}\beta$  carbons which are most sensitive to the conformation. This proves that the secondary structure of the C-ter HsCen2/P17-XPC complex is very similar in solution and in microcrystalline states.

The conformational flexibility of the backbone has been probed through relaxation-compensated measurements of dipolar order parameters in constant-time cross-polarization experiments. The dipolar coupling constants and order parameters reveal increased overall conformational flexibility of the EF-III, EF-IV, and linker loops, except for residues involved in the coordination of  $\text{Ca}^{2+}$  cations that stabilize the hydrophobic pocket containing the peptide P17-XPC.

The strategy applied in this work is expected to be useful to obtain structural and motional information in other microcrystalline proteins and their complexes as well as other classes of biopolymers.

#### ■ ASSOCIATED CONTENT

##### ● Supporting Information

Seven figures, two tables, protein expression and purification protocols, and the preparation of solutions of the complex. This material is available free of charge via the Internet at <http://pubs.acs.org>.

#### ■ AUTHOR INFORMATION

##### Corresponding Author

\*E-mail: Piotr.Tekely@ens.fr.

##### Notes

The authors declare no competing financial interest.

#### ■ ACKNOWLEDGMENTS

Financial support from the Agence Nationale de la Recherche (Project “FastSpinProts” ANR-09-BLAN-0111-01) and from the CNRS, INSERM, Institut Curie, and ENS is gratefully acknowledged. We also thank Dr. Anja Böckmann for valuable assistance during the filling of the rotors.

#### ■ REFERENCES

- (1) Araki, M.; Masutani, C.; Takemura, M.; Uchida, A.; Sugawara, K.; Kondoh, J.; Ohkuma, Y.; Hanaoka, F. *J. Biol. Chem.* **2001**, 276, 18665–18672.

- (2) Nishi, R.; Okuda, Y.; Watanabe, E.; Mori, T.; Iwai, S.; Masutani, C.; Sugawara, K.; Hanaoka, F. *Mol. Cell. Biol.* **2005**, *25*, 5664–5674.
- (3) Tourbez, M.; Firanescu, C.; Yang, A.; Unipan, L.; Duchambon, P.; Blouquit, Y.; Craescu, C. T. *J. Biol. Chem.* **2004**, *279*, 47672–47680.
- (4) Yang, A.; Miron, S.; Duchambon, P.; Assairi, L.; Blouquit, Y.; Craescu, C. T. *Biochemistry* **2006**, *45*, 880–889.
- (5) Matei, E.; Miron, S.; Blouquit, Y.; Duchambon, P.; Durussel, I.; Cox, J. A.; Craescu, C. T. *Biochemistry* **2003**, *42*, 1439–1450.
- (6) Popescu, A.; Miron, S.; Blouquit, Y.; Duchambon, P.; Craescu, C. T. *J. Biol. Chem.* **2003**, *278*, 40252–40621.
- (7) Yang, A.; Miron, S.; Mouawad, L.; Duchambon, P.; Blouquit, Y.; Craescu, C. T. *Biochemistry* **2006**, *45*, 3653–3663.
- (8) Durussel, I.; Blouquit, Y.; Middendorp, S.; Craescu, C. T.; Cox, J. A. *FEBS Lett.* **2000**, *472*, 208–212.
- (9) *Solid-state NMR Studies of Biopolymers*; McDermott, A. E., Polenova, T., Eds.; J. Wiley & Sons Ltd: Chichester, U.K., 2010.
- (10) Lange, A.; Giller, K.; Hornig, S.; Martin-Eauclaire, M. F.; Pongs, O.; Becker, S.; Baldus, M. *Nature* **2006**, *440*, 959–962.
- (11) Sperling, L. J.; Berthold, D. A.; Sasser, T. L.; Jeisy-Scott, V.; Rienstra, C. M. *J. Mol. Biol.* **2010**, *399*, 268–282.
- (12) Chan-Huot, M.; Duma, L.; Charbonnier, J. B.; Herbert-Pucheta, J. E.; Assairi, L.; Blouquit, Y.; Abergel, D.; Bodenhausen, G. *Cryst. Growth Des.* [Online early access]. DOI: 10.1021/cg301378j. Published Online: Nov 5, **2012**.
- (13) Böckmann, A.; Gardiennet, C.; Verel, R.; Hunkeler, A.; Loquet, A.; Pintacuda, G.; Emsley, L.; Meier, B. H.; Lesage, A. *J. Biomol. NMR* **2009**, *45* (3), 319–327.
- (14) Potrzebowski, M. J.; Tekely, P.; Dusauroy, Y. *Solid State Nucl. Magn. Reson.* **1998**, *11*, 253–257.
- (15) Tekely, P.; Montigny, F.; Canet, D.; Delpuech, J. J. *Chem. Phys. Lett.* **1990**, *175*, 401–406.
- (16) Palmas, P.; Tekely, P.; Canet, D. *J. Magn. Reson.* **1993**, *104*, 26–36.
- (17) Tekely, P.; Gérardy, V.; Palmas, P.; Canet, D.; Retournard, A. *Solid State Nucl. Magn. Reson.* **1995**, *4*, 361–367.
- (18) Klur, I.; Jacquinet, F. J.; Brunet, F.; Charpentier, T.; Virlet, J.; Schneider, C.; Tekely, P. *J. Phys. Chem. B* **2000**, *104*, 10162–10167.
- (19) Weingarth, M.; Demco, D. E.; Bodenhausen, G.; Tekely, P. *Chem. Phys. Lett.* **2009**, *469*, 342–348.
- (20) (a) Weingarth, M.; Tekely, P.; Bodenhausen, G. *Chem. Phys. Lett.* **2009**, *466*, 247–251. (b) Weingarth, M.; Bodenhausen, G.; Tekely, P. *J. Magn. Reson.* **2009**, *199*, 238–241. (c) Weingarth, M.; Bodenhausen, G.; Tekely, P. *Chem. Phys. Lett.* **2011**, *502*, 259–265.
- (21) Tekely, P.; Palmas, P.; Canet, D. *J. Magn. Reson., Ser. A* **1994**, *107*, 129–133.
- (22) Veshtort, M.; Griffin, R. G. *J. Magn. Reson.* **2006**, *178*, 248–282.
- (23) Gardiennet, C.; Marica, F.; Fyfe, C. A.; Tekely, P. *J. Chem. Phys.* **2005**, *122*, 054705.
- (24) Pauli, J.; van Rossum, B.; Forster, H.; de Groot, H. J. M.; Oschkinat, H. *J. Magn. Reson.* **2000**, *143*, 411–416.
- (25) Martin, R. W.; Zilm, K. W. *J. Magn. Reson.* **2003**, *165*, 162–174.
- (26) Böckmann, A.; Lange, A.; Galinier, A.; Luca, S.; Giraud, N.; Juy, M.; Heise, H.; Montserret, R.; Penin, F.; Baldus, M. *J. Biomol. NMR* **2003**, *27*, 323–339.
- (27) Igumenova, T. I.; Wand, A. J.; McDermott, A. E. *J. Am. Chem. Soc.* **2004**, *126*, 5323–5331.
- (28) Seidel, K.; Etzkorn, M.; Heise, H.; Becker, S.; Baldus, M. *ChemBioChem* **2005**, *6*, 1638–1647.
- (29) Schneider, R.; Seidel, K.; Etzkorn, M.; Lange, A.; Becker, S.; Baldus, M. *J. Am. Chem. Soc.* **2010**, *132*, 223–233.
- (30) Mielczarski, J. A.; Cases, J. M.; Tekely, P.; Canet, D. *Langmuir* **1993**, *9*, 3357–3370.
- (31) Chevelkov, V.; Faelber, K.; Diehl, A.; Heinemann, U.; Oschkinat, H.; Reif, B. *J. Biomol. NMR* **2005**, *31*, 295–310.
- (32) Weingarth, M.; Bodenhausen, G.; Tekely, P. *J. Am. Chem. Soc.* **2009**, *131*, 13937–13939.
- (33) Weingarth, M.; Masuda, Y.; Takegoshi, K.; Bodenhausen, G.; Tekely, P. *J. Biomol. NMR* **2011**, *50*, 129–136.
- (34) Herbert-Pucheta, J. E.; Colaux, H.; Bodenhausen, G.; Tekely, P. *J. Phys. Chem. B* **2011**, *115*, 15415–15421.
- (35) Herbert-Pucheta, J. E.; Pelupecy, P.; Bodenhausen, G.; Tekely, P. *Chem. Phys. Lett.* **2012**, *539–540*, 245–251.
- (36) Charbonnier, J. B.; Renaud, E.; Miron, S.; Le Du, M. H.; Blouquit, Y.; Duchambon, P.; Christova, P.; Shosheva, A.; Rose, T.; Angulo, J. F.; Craescu, C. T. *J. Mol. Biol.* **2007**, *373*, 1032–1046.
- (37) Torchia, D. A.; Szabo, A. *J. Magn. Reson.* **1985**, *64*, 135–141.
- (38) Hong, M.; Yao, X.; Jakes, K.; Huster, D. *J. Phys. Chem. B* **2002**, *106*, 7355–7364.
- (39) Lorieau, J. L.; McDermott, A. E. *J. Am. Chem. Soc.* **2006**, *128*, 11505–11512.
- (40) Franks, W. T.; Zhou, D. H.; Wylie, B. J.; Money, B. G.; Graesser, D. T.; Frericks, H. L.; Sahota, G.; Rienstra, C. M. *J. Am. Chem. Soc.* **2005**, *127*, 12291–12305.
- (41) Chevelkov, V.; Fink, U.; Reif, B. *J. Am. Chem. Soc.* **2009**, *131*, 14018–14022.
- (42) Schanda, P.; Meier, B. H.; Ernst, M. *J. Am. Chem. Soc.* **2010**, *132*, 15957–15967.
- (43) Müller, L.; Kumar, A.; Baumann, T.; Ernst, R. R. *Phys. Rev. Lett.* **1974**, *32*, 1402–1406.
- (44) Pines, A.; Gibby, M. G.; Waugh, J. S. *J. Chem. Phys.* **1973**, *59*, 569–590.
- (45) Palmas, P.; Malveau, C.; Tekely, P.; Canet, D. *Solid State Nucl. Magn. Reson.* **1998**, *13*, 45–53.
- (46) Hester, R.; Ackerman, J.; Cross, V.; Waugh, J. S. *Phys. Rev. Lett.* **1975**, *34*, 993–995.
- (47) Roberts, J. E.; Harbison, G. S.; Munowitz, M. G.; Herzfeld, J.; Griffin, R. G. *J. Am. Chem. Soc.* **1987**, *109*, 4163–4169.
- (48) Gardiennet, C.; Tekely, P. *J. Phys. Chem. B* **2002**, *106*, 8928–8936.
- (49) Tekely, P.; Brondeau, J.; Elbayed, K.; Retournard, A.; Canet, D. *J. Magn. Reson.* **1988**, *80*, 509–516.
- (50) Scilab, a free scientific software package. INRIA ENPC, www.scilab.org (1989–2005).
- (51) Lipari, G.; Szabo, A. *J. Am. Chem. Soc.* **1982**, *104*, 4546–4559.